FULL PAPER

Transparent Conductors

ADVANCED
ELECTRONIC
MATERIALS
www.advelectronicmat.de

Design of n-Type Transparent Conducting Oxides: The Case of Transition Metal Doping in In$_2$O$_3$

Jian Xu, Jian-Bo Liu, Bai-Xin Liu,* Shun-Ning Li, Su-Huai Wei,* and Bing Huang*

Design of novel n-type transparent conducting oxides beyond Sn-doped In$_2$O$_3$ has stimulated extensive interest in the past decade. One of the approaches can be using transition metals (TMs) as dopants. In this article, using In$_2$O$_3$ as an example, it is shown that TM doping in oxides can be classified into three categories (type-I, II, or III) based on their TM d-orbital energy levels reference to the bottom of the conduction band of In$_2$O$_3$. It is found that although Mo is proposed to replace Sn as a promising TM donor to achieve higher carrier density in In$_2$O$_3$, it actually exhibits unusual dual-doping behaviors, i.e., it can act as either a deep donor when it occupies the In 8b-sites (type-I) or shallow single donor when it occupies the In 24d-sites (type-II). The calculated ionization of Mo in In$_2$O$_3$ increases as the growth temperature increases, in good agreement with experimental observations but contradict to previous theoretical studies. It is also identified that Zr, Hf, and Ta (type-III) are better potential donors than Mo and Sn in In$_2$O$_3$ for achieving higher carrier mobility and density. The analysis and approach can also be used to improve the doping performance in other oxides.

1. Introduction

Sn-doped In$_2$O$_3$ (ITO) is widely used as a n-type transparent conducting oxide (TCO) for many emerging optoelectronic applications, e.g., flat panel displays, solar cells, low thermal emissivity coatings, light emitting diodes, and smart windows.[1–6] However, the strong orbital hybridization between the Sn and In 5s states at the bottom of conduction band (CB) of In$_2$O$_3$ can significantly renormalize its band curvature (**Figure 1**a), thus may reduce the intrinsic carrier (electron) mobility (μ_e) upon doping because of the increased electron effective mass (m_e).[7,8] Moreover, since each Sn dopant can only donate (maximum) one excess electron into In$_2$O$_3$, sufficiently high density of Sn is required to achieve high carrier (electron)

density (n_e). Therefore, it is highly desired to design alternative dopants in In$_2$O$_3$ that can achieve higher μ_e and n_e than that of Sn.

Generally speaking, an ideal n-type dopant that can maintain high μ_e and donate sufficient electrons n_e into the CB of In$_2$O$_3$ should have its donor level high inside the CB of the In$_2$O$_3$ (Figure 1b). It is expected that some transition-metal (TM) atoms might be the targeted dopants because the TM d orbitals may have sufficiently higher orbital energies than that of In 5s orbitals and they naturally may have multiple valence-electrons that can be effectively doped to the CB of In$_2$O$_3$ to make it n-type. Moreover, differing from Sn, the orbital hybridization between TM d orbitals and In 5s orbitals is weak under the crystal symmetry of In$_2$O$_3$. As a result, the band curvature, i.e., m_e around the CB minimum (CBM) of In$_2$O$_3$, could be largely maintained. In real situations, the μ_e of materials depends on the relaxation time (τ), the electronic charge (q) and m_e in the conduction band by following the relationship: $\mu_e = q\tau/m_e$. Therefore, μ_e can be increased by increasing τ or by decreasing m_e. Increasing τ requires the decrease of impurity scattering, lattice distortion scattering, acoustic phonon scattering, longitudinal optical phonon scattering, etc.[9–11] Decreasing m_e requires the increase of CBM band edge dispersion. Since TM doping may reduce m_e and impurity scattering (for the same carrier density, the required TM dopant density is less than that of Sn), it is reasonable to expected that μ_e could be increased by TM doping.

In recent years, there has been growing interests in searching ideal TM dopants for n-type In$_2$O$_3$.[12–23] For example, Mo-doped In$_2$O$_3$ (IMO) has attracted particular attention due to its high miscibility and possibility to reach high n_e and μ_e.[24–27] However, it is found that the μ_e and n_e of IMO films strongly depend on their growth temperatures (GT). For example, when the GT increases from 298 to 723 K, the μ_e (n_e) of IMO films can dramatically increase from 10 cm^2 V^{-1} s^{-1} (6×10^{19} cm^{-3}) to 119 cm^2 V^{-1} s^{-1} (7×10^{20} cm^{-3}).[2,26,28–31] Although some first-principles calculations have been carried out to understand the electronic properties of IMO,[26,32] this puzzling experimental phenomena of GT-dependent electronic properties has not been explained thus far. It is also not clear whether other TM dopants can give better doping properties than Mo.

In this article, based on first-principles hybrid functional (HSE06) calculations, we have systemically investigated the

Dr. J. Xu, Prof. J.-B. Liu, Prof. B.-X. Liu, Dr. S.-N. Li
Key Laboratory of Advanced Materials (MOE)
School of Materials Science and Engineering
Tsinghua University
Beijing 100084, China
E-mail: dmslbx@mail.tsinghua.edu.cn
Dr. J. Xu, Prof. S.-H. Wei, Prof. B. Huang
Beijing Computational Science Research Center
Beijing 100193, China
E-mail: suhuaiwei@csrc.ac.cn; bing.huang@csrc.ac.cn

The ORCID identification number(s) for the author(s) of this article can be found under https://doi.org/10.1002/aelm.201700553.

**ADVANCED
SCIENCE NEWS**
www.advancedsciencenews.com

**ADVANCED
ELECTRONIC
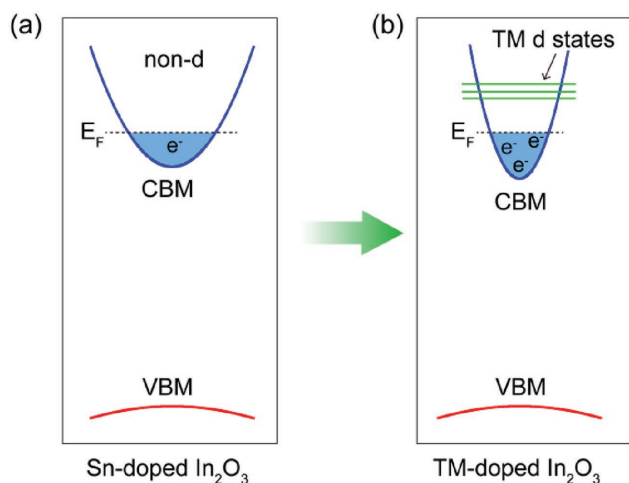MATERIALS**
www.advelectronicmat.de

Figure 1. Schematic diagram of the band structures for a) Sn-doped and b) ideal TM-doped In_2O_3. The Fermi level (E_F) is marked by dashed line.

general doping behaviors of TM atoms in In_2O_3. Interestingly, it is found that although the ground-state doping configuration of Mo in In_2O_3 is a deep donor, its metastable doping configuration, whose defect density can be significantly increased as the GT increases, is a shallow donor that can effectively make In_2O_3 n-type. We show that, in terms of the TM d-orbital energy

levels referenced to the CBM of In_2O_3, the doping behaviors of TM in In_2O_3 can be classified into three types. Based on this understanding, we have successfully found that some TM atoms such as Zr, Hf, and Ta are better shallow donors than Sn to realize higher μ_e and n_e in In_2O_3.

2. Results and Discussions

The HSE06-calculated lattice parameter and fundamental bandgap ($E_g = 2.78$ eV) of In_2O_3 agrees well with the experimental results (see the Experimental Section). As shown in **Figure 2**a, in cubic In_2O_3 (bixbyite structure) there are two inequivalent cation sites: 25% cations (8b site) occupy the centers of the trigonally distorted octahedral, while the other 75% cations (24d site) are coordinated to six anions in tetragonally distorted octahedral. A 40-atom primitive cell of In_2O_3 is selected for the doping calculation (equal to a doping concentration of 6.25%, within the solubility range of In_2O_3 in the experiments[6,13]). Our test calculations confirm that the calculated defect properties are not sensitive to the supercell size and spin-orbit coupling effect (see Figures S1 and S2 in the Supporting Information). It is interesting to see that the formation energies (E^f) of TM dopants under O-poor conditions are lower than that under O-rich conditions (see Table S3 in the Supporting Information). This unusual trend is because under
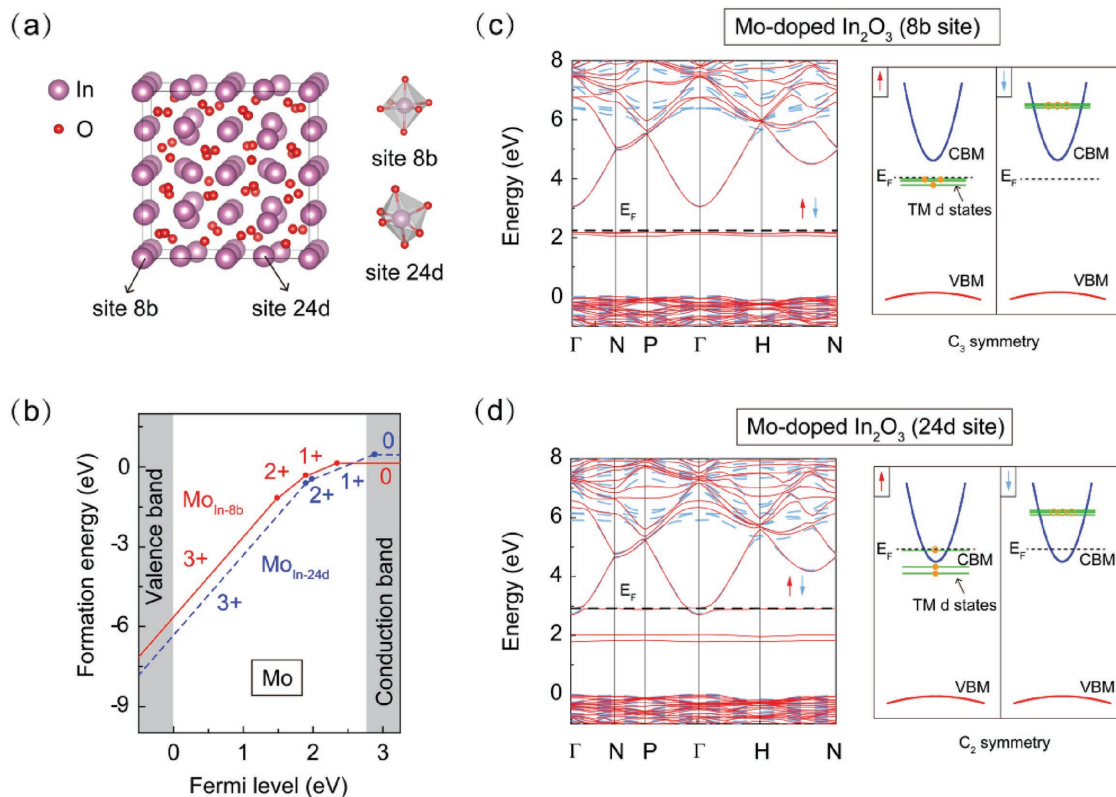

Figure 2. a) Crystal structure of bulk bixbyite In_2O_3. Two inequivalent local In sites (site 8b and site 24d in Wyckoff notion) are labeled herein. b) Calculated formation energies (E^f) of Mo_{In-8b} and Mo_{In-24d} at different charge states as a function of E_F under O-poor conditions. The solid and dashed lines represent Mo_{In-8b} and Mo_{In-24d} cases, respectively. c) HSE06-calculated band structure (left panel) for the case of Mo_{In-8b}. Schematic diagram of d-orbital defect levels (right panel) in the case of Mo_{In-8b} (only the three critical d-orbitals are plotted here). d) Same as (c) but for the case of Mo_{In-24d}. The spin-up and spin-down channels are illustrated in red-solid and blue-dashed lines, respectively.
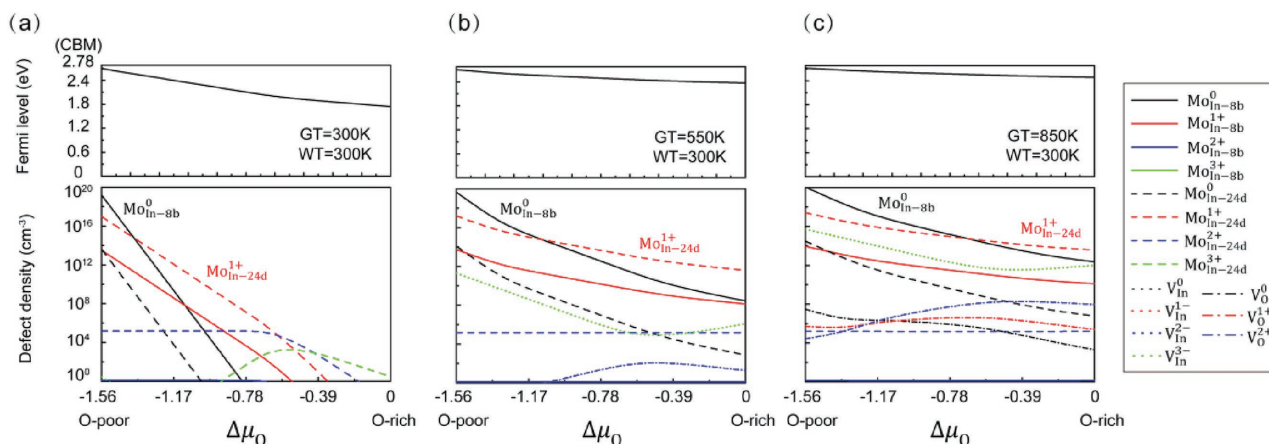
Figure 3. a–c) Calculated defect densities and E_F positions a function of $\Delta\mu_O$ for Mo-doped In_2O_3 (at both $Mo_{In\text{-}8b}$ and $Mo_{In\text{-}24d}$ sites) for the growth temperatures of 300, 550, and 850 K, respectively. The working temperature is set to 300 K. The low-energy donor V_O and acceptor V_{In} in In_2O_3 are also considered in the calculations.

O-poor condition, the increase of the chemical potential of the dopant is faster than that of In. The only exception is for the case of Cr, which is caused by the choice of chemical potential regions to avoid the formation of the competing secondary phases (see Table S2 in the Supporting Information).

First, we focus on the case of Mo-doped In_2O_3, which has attracted great attention before.[2,24–26,28–32] Our defect E^f calculations confirm that Mo substitutional doping of In (Mo_{In}) dominates over oxygen vacancies (V_O) and Mo interstitials (Mo_i) (see Figure S3 in the Supporting Information). According to our total energy calculations, $Mo_{In\text{-}8b}$ is energetically more stable than $Mo_{In\text{-}24d}$ by 0.36 eV/Mo in nominally neutral charge state, as shown in Figure 2b. After replace In, one Mo_{In} has three remaining d electrons, which can exhibit either high-spin configuration ($d^3\uparrow d^0\downarrow$) or low-spin configuration ($d^2\uparrow d^1\downarrow$), depending on the relative energy sizes of its crystal field splitting (Δ_{cf}) and exchange splitting (Δ_{ex}).[33]

For $Mo_{In\text{-}8b}$, the Jahn–Teller distortion induced by structural relaxation can reduce its local symmetry from T_h to C_3, therefore, the triple-degenerate t_2 d-levels split into two double-degenerate states e and a single state a, as illustrated in Figure 2c. Because of $\Delta_{ex} > \Delta_{cf}$, our HSE06 calculations demonstrate that the $d^3\uparrow d^0\downarrow$ configuration is the ground-state electronic structure of $Mo_{In\text{-}8b}$ (the total energy of $d^3\uparrow d^0\downarrow$ configuration is 1.34 eV/Mo lower than that of $d^2\uparrow d^1\downarrow$ configuration), agreeing with the conclusion obtained from the local density approximation (LDA)/Perdew-Burke-Ernzerhof (PBE) calculations (see Figure S4 in the Supporting Information).[32] The Δ_{ex} between spin-up and spin-down electrons will push the spin-up (spin-down) a and e states down (up) inside the bandgap (conduction band) and become occupied (unoccupied). As a result, the three occupied d electrons deep inside the bandgap in spin-up channel makes $Mo_{In\text{-}8b}$ as a deep donor, whose 0/+1 charge transition level (CTL) is ≈0.4 eV below the CBM, as shown in Figure 2b. However, the LDA/PBE level calculations incorrectly give rise to the shallow defect levels of $Mo_{In\text{-}8b}$ due to the largely underestimated In_2O_3 bandgap.[32] Moreover, we want to emphasize that the conclusions drawn by Bhachu et al.[26] based on HSE06 calculations were not convinced since they failed to determine the stable ground-state spin configuration of IMO.

For metastable $Mo_{In\text{-}24d}$ where cations are coordinated to six anions in a more distorted octahedral, its local symmetry is further reduced to C_2 after structural relaxation. The double-degenerated e states further split into two single a′ and b states, and the occupied a′ state in spin-up channel is pushed up above the CBM, as illustrated in Figure 2d. Therefore, $Mo_{In\text{-}24d}$ can behave as a shallow donor with 0/+1 CTL even above CBM, as shown in Figure 2b. As a result, Mo in In_2O_3 can surprisingly exhibit a dual-doping behavior depending on its doping site.

To understand the GT-dependent μ_e and n_e in IMO, we have self-consistently calculated the defect densities of $Mo_{In\text{-}8b}$ and $Mo_{In\text{-}24d}$ along with other dominant intrinsic defects (V_O and V_{In}) as a function of the GT and the oxygen chemical potential ($\Delta\mu_O$), as shown in **Figure 3**. Generally, the defects can be created at the GT, whose total densities strongly depend on the GT; after quench to the working temperature (WT), the charge states between these defects along with the equilibrium Fermi level (E_F) in the system will be redistributed, but the total defect densities maintain the same as that created in the GT (see the Experimental Section). When $\Delta\mu_O$ increases, as shown in Figure 3, the equilibrium E_F gradually shifts away from the CBM of In_2O_3. Consequently, the most dominant defect would be changed from $Mo^0_{In\text{-}8b}$ (neutral deep-donor) to $Mo^{1+}_{In\text{-}24d}$ (ionized shallow-donor) as $\Delta\mu_O$ increases at each GT, consistent with the CTL analysis (Figure 2b). More importantly, the $Mo^{1+}_{In\text{-}24d}$ density can be strongly enhanced as the GT increases, because more Mo will occupy In_{24d} site when GT is high. For example, it increases from 10^7 cm^{-3} (GT = 300 K) to 10^{13} cm^{-3} (GT = 550 K) to 10^{18} cm^{-3} (GT = 850 K) when $\Delta\mu_O = -0.78$ eV (a middle value in the range of $\Delta\mu_O$) and this value could be much higher at the O-poor condition. As a result, the E_F of the system can be upshifted closer to the CBM in the whole $\Delta\mu_O$ range, as the GT increases. Thus, our finding can generally explain the trend of GT-dependent electronic properties of IMO, as observed in the experiments.[2,26,28–31]

The above discussions demonstrate that Mo is not an ideal TM donor in In_2O_3 and its doping performance strongly depends on the GT. It is therefore highly desirable to search alternative high-efficient TM donors that can dope sufficient
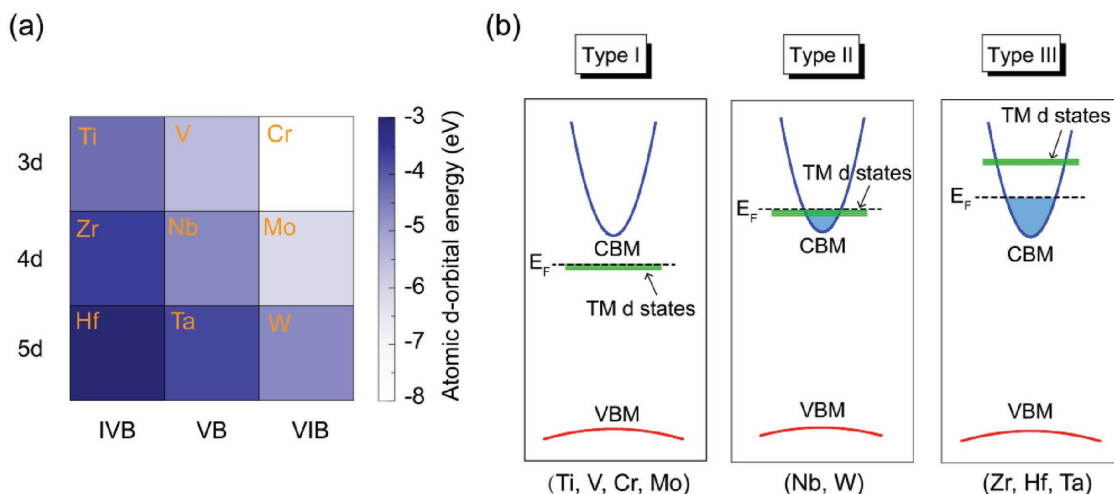
**ADVANCED
SCIENCE NEWS**

www.advancedsciencenews.com

**ADVANCED
ELECTRONIC
MATERIALS**

www.advelectronicmat.de

Figure 4. a) Atomic d-orbital energy for neutral transition metal atoms X (X = Ti, Zr, Hf, V, Nb, Ta, Cr, Mo, W). b) Schematic diagrams of band structures for type-I (left), type-II (middle), and type-III (right) TM-doped In_2O_3. The E_F is indicated as dashed line.

electrons to In_2O_3 at its ground-state doping configuration. It is expected that a TM donor with higher d orbital energies than that of Mo might give rise to shallower defect levels even at its ground-state configuration. As shown in **Figure 4**a, for TM elements in the same period of periodic table the atomic d-orbital energy level would decreases with increasing atomic number, while an increasing energy level is observed in the same column when atomic number increases. To develop our understanding of the general doping behaviors of TM atoms in In_2O_3, we have systemically studied all the nine potential donor elements selected in Figure 4a. It is well known that most of the TMs are earth abundant, same as Sn, so earth abundance and price are not the concern for the selection of TM dopants to replace Sn.

Generally, at the ground-state, whether TM substituting In in In_2O_3 at In_{8b} or In_{24d} site is determined by the energy competition between the energy-gain from the crystal field splitting (ΔE_{cf}) and the energy-loss from the strain energy (ΔE_s) at In_{24d} site (with a larger structural distortion), which is similar to the formation of DX-center in semiconductors.[34] For Cr, Mo, and W (same column in Figure 4a), e.g., as shown in Figure 2, the three defect levels are all occupied (in spin-up channel) by the three TM d-electrons, thus the level splitting at the In_{24d} site due to structural-distortion does not gain energy, therefore, it results in a more favorable doping site of In_{8b} in In_2O_3 (see Table S3 in the Supporting Information). For V, Nb, and Ta, they contain one less electron than Mo, so after relaxation at In_{24d} doping site, the two TM d-electrons will occupy the lowest-energy levels whereas the high energy level will be empty, which results in an energy-preference at In_{24d} site because of $\Delta E_{cf} > \Delta E_s$ (see Table S3 in the Supporting Information). For Ti, Zr, and Hf, they have only one extra electron to donate, so the low energy crystal-field-split TM d levels are not fully occupied. In this case the energy-gain ΔE_{cf} may not be sufficient for $\Delta E_{cf} > \Delta E_s$. For example, compared to Zr and Hf, the smaller atomic size of Ti doping at In_{24d} site can induce a larger ΔE_s and $\Delta E_{cf} < \Delta E_s$, as a result, Ti (Zr or Hf) favors the In_{8b} (In_{24d}) site.

In terms of their ground-state electronic structures, we find that these TM dopants can be generally classified into three

types, denoted as type-I, type-II, and type-III. Type-I donors (Ti, V, Cr, and Mo): In this case, the d-orbital defect levels are significantly lower in energy than the CBM of In_2O_3 (Figure 4b, left panel), consequently, effective n-type doping cannot be achieved at room temperature. Type-II donors (Nb and W): In this case, the d-orbital defect levels are above the CBM of In_2O_3, but because they are not high enough in energy (Figure 4b, middle panel), the TM d bands will merge with the occupied CB when the system is heavily doped, so that E_F will be pinned by the partially occupied d levels. Although n-type doping can be achieved, the n_e and μ_e will be low due to the large effective mass of the TM d band. Type-III donors (Zr, Hf, and Ta): In this case, the d-orbital defect levels are sufficiently high in energy above the CBM of In_2O_3, so that TM dopants can be fully ionized (Figure 4b, right panel) and the μ_e can be largely maintained; therefore, ideal n-type doping could be realized with high μ_e and n_e (Figure 1b).

From the case of Mo doping, we can understand that the strong GT-dependent TM doping performance usually can occur in these TM dopants behaving unusual dual-doping behaviors. Among other three type-I TM dopants (Ti, V, and Cr), only Ti exhibits this unusual dual-doping behavior (see Figure S5 in the Supporting Information), and therefore it is reasonable to expect that a GT-dependent doping performance can occur in Ti-doped In_2O_3. For other type-II donors (Nb and W) and type-III donors (Zr, Hf, and Ta), they do not have such dual-doping behaviors so it is expected that there will be no strong GT-dependent doping performance for them. Another typical type-II donor is Nb (**Figure 5**a). For Nb_{In}, the occupied d defect levels are above the CBM because Nb d level is higher in energy than Mo, which makes Nb_{In-24d} a resonant donor, as shown in CTL in Figure 5b. Unfortunately, since the defect d levels are not sufficiently high in energy compared to CBM, the two d-levels cannot be fully ionized after charge transfer, which can pin the E_F to the position of partially occupied d-orbital defect level (the maximum n_e obtained from Nb-doped In_2O_3 is ≈10^{21} cm^{-3}, comparable to the n_e of an ideal TCO). Thus, although ideal n_e can be obtained, the μ_e of the system may decrease due to the high effective mass near the E_F. The doping

**ADVANCED
SCIENCE NEWS**
www.advancedsciencenews.com

**ADVANCED
ELECTRONIC
MATERIALS**
www.advelectronicmat.de

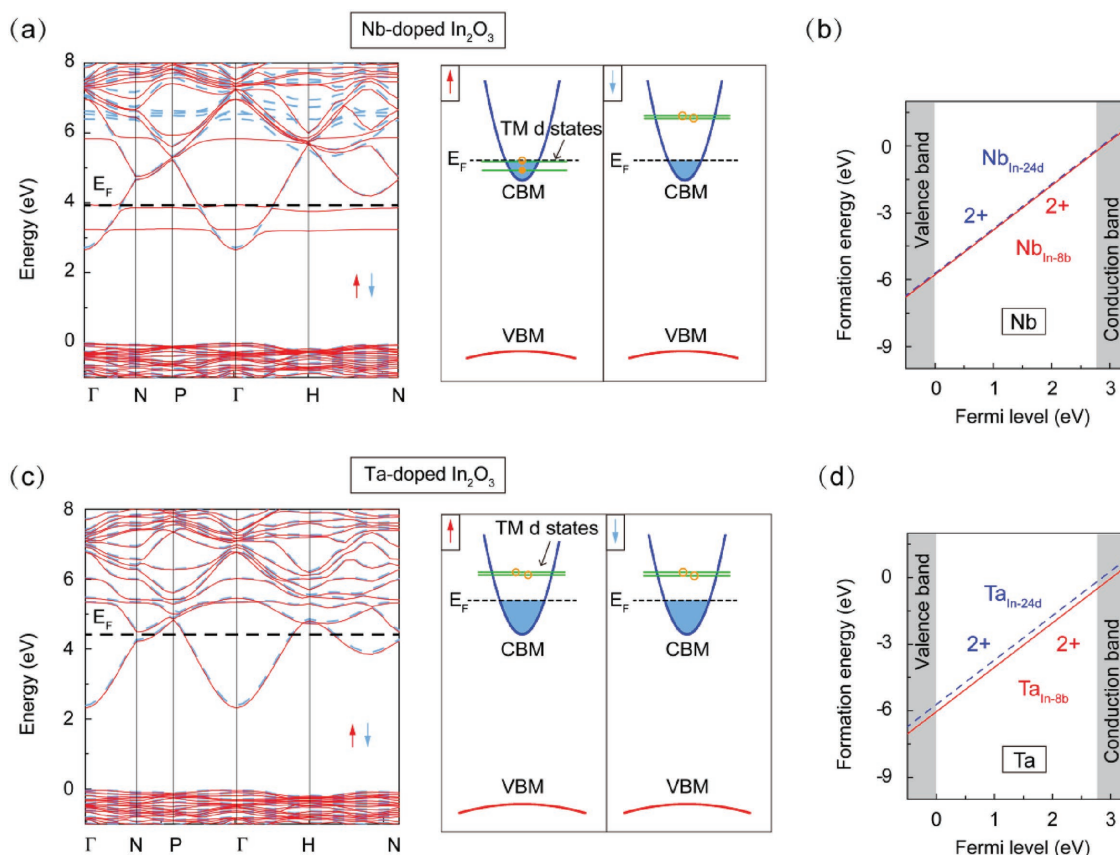**Figure 5.** a) HSE06-calculated band structure (left panel) for the case of Nb_{In-24d} (ground-state). Schematic diagram of d-orbital defect levels (right panel) in the case of Nb_{In-24d} (only the two critical d-orbitals are plotted here). b) Calculated E^f of Nb_{In-8b} and Nb_{In-24d} with different charge states q as a function of the E_F under O-poor conditions. The red-solid and blue-dashed lines represent Nb_{In-8b} and Nb_{In-24d} cases, respectively. (c) and (d) are for the Ta-doped In_2O_3 cases.

behavior of W in In_2O_3 is similar to that of Nb (see Figure S6 in the Supporting Information).

Finally, we turn to the doping case of type-III, which can give the best doping performance (Figure 1b). Taking Ta as an example, since 5d orbital has much smaller exchange splitting than 3d or 4d elements, we find $\Delta_{ex} < \Delta_{cf}$ (ground-state), and thus Ta_{In-24d} favors the low spin-configuration of $d^1\uparrow d^1\downarrow$, as shown in Figure 5c. More importantly, the localized 5d defect states of Ta_{In-24d} are located >3 eV above the CBM, so that Ta can be fully ionized and the band dispersion around the CBM of In_2O_3 is not modified after Ta doping, e.g., the calculated m_e around the CBM of In_2O_3 is 0.22 (0.21) m_0 before (after) Ta doping (see Table S4 in the Supporting Information). Therefore, it is expected that the n_e in In_2O_3 films increase upon Ta doping, meanwhile the μ_e of In_2O_3 can be largely maintained. This is in contrast to ITO, where the strong hybridization of Sn 5s-orbitals with In 5s-orbitals (Figure 1a) results in a significantly enlarged m_e of $\approx 0.41m_0$ around the CBM at a Sn doping concentration of 6.25%, which agrees well with the theoretical and experimental measurements of up to 0.40 m_0.[7,8,35] The doping behaviors of Zr and Hf are similar to that of Ta (see Figure S7 in the Supporting Information). Moreover, the calculated E^f of Zr^0_{In-24d} and Hf^0_{In-24d} are comparable to that of Sn^0_{In-8b} under O-poor condition (see Table S3 in the Supporting

Information), indicating that they can reach sufficient dopant densities in In_2O_3.[19,21,22] Our theories can explain the experimental observation that Zr has a superior performance (high mobility and high carrier densities) than Sn in In_2O_3.[19,21,22,36–38] Generally, it is found that the defect energy levels of all these TM dopants in In_2O_3 follow the atomic d-orbital energy trends shown in Figure 4a (see Figure S8 in the Supporting Information).

3. Conclusion

In conclusion, we have systemically investigated the general doping behaviors of TM atoms in In_2O_3. We have demonstrated the unusual role of Mo in In_2O_3. Moreover, we find that the doping behaviors of TM atoms in In_2O_3 can be generally classified into three categories in terms of d-orbital energy level referenced to the CBM. Based on this characterization, we have successfully found that some TM atoms (type-III donors) such as Zr, Hf, and Ta are better shallow donors than Sn to realize higher μ_e and n_e in In_2O_3. Therefore, our study not only has clarified a long-standing debate that whether or not Mo is a good dopant for n-type In_2O_3, but also provides a general guideline for the selection of suitable TM dopants to achieve higher

**ADVANCED
SCIENCE NEWS**

www.advancedsciencenews.com

**ADVANCED
ELECTRONIC
MATERIALS**

www.advelectronicmat.de

n_e and maintain the high μ_e and optical transparency of TCOs. Our study may also be applied to design ideal dopants in other oxides.

4. Experimental Section

Computational Details: All calculations were carried out using the Vienna Ab initio Simulation Package.[39] The electron-ion interactions were described by the projector augmented wave method,[40,41] while the exchange-correlation energy was treated with the screened HSE06 hybrid density functional.[42,43] In HSE06 calculations,[44] the screening parameter was set to 0.2 Å^{-1} and the standard exchange mixing was taken, i.e., keeping 25% of Hartree–Fork exchange and 75% of PBE-the generalized gradient approximation (GGA) exchange. A kinetic-energy cutoff of 400 eV was tested to be sufficient for plane-waves expansion to achieve good convergence. During all the structural relaxations, a conjugate gradient algorithm was used until the force on each atom was less than 0.02 eV Å^{-1} and the total energy was converged to 1.0×10^{-5} eV. The HSE06 calculated equilibrium lattice parameter (a) of cubic In_2O_3 was 10.10 Å, and the direct fundamental bandgap (E_g) of the primitive cell was 2.78 eV, agreeing well with the experimental results ($a = 10.12$ Å;[45] $E_g = 2.70$ eV,[46] 2.90 eV[47]) and previous HSE06 calculations ($a = 10.16$ Å;[26] $E_g = 2.75$ eV,[26] 2.74 eV[48]).

Defect Thermodynamics: The defect formation energy can be evaluated as[49,50]

$$E^f\left[X^q\right] = E_{tot}\left[X^q\right] - E_{tot}[P] + \sum_i n_i \mu_i + q\left(\varepsilon_{VBM} + E_F\right) + E_{align}\left[X^q\right] \quad (1)$$

where $E_{tot}[X^q]$ is the total energy of a supercell containing the defect X in charge state q, and $E_{tot}[P]$ is the total energy of the corresponding pristine bulk lattice. n_i is the number of atoms being removed from ($n_i > 0$) or added to ($n_i < 0$) the supercell, and μ_i denotes the corresponding chemical potential. ε_{VBM} and E_F are the energy levels corresponding to the valence band maximum (VBM) and the Fermi level measured from the VBM, respectively. Additionally, $E_{align}[X^q]$ (i.e., $q\Delta V$) is a potential-alignment correction term to correct for the finite-size effects in the calculations of charged defects, and this term is determined by aligning the core levels of atoms far from the defect center in defective cells to that of the pristine bulk.[51,52] Charge-state transition levels were also examined, which are defined as[53–55]

$$\varepsilon\left(q_1/q_2\right) = \frac{\left(E_{tot}\left[X^{q_1}\right] + E_{align}\left[X^{q_1}\right]\right) - \left(E_{tot}\left[X^{q_2}\right] + E_{align}\left[X^{q_2}\right]\right)}{q_2 - q_1} - \varepsilon_{VBM} \quad (2)$$

These CTLs correspond to the Fermi-level positions at which X changes its charge state. $E_{tot}[X^{q_1}]$ and $E_{tot}[X^{q_2}]$ are the total energies of a supercell containing the defect X in charge state q_1 and q_2, respectively. $E_{align}[X^{q_1}]$ and $E_{align}[X^{q_2}]$ are the potential-alignment correction terms to correct for the finite-size effects in the calculations of charged defects X^{q_1} and X^{q_2}, respectively. The CTLs are independent of the selected μ_i (see the Supporting Information for more detailed physical explanations of CTLs).

Two limiting conditions were considered in this work, i.e., O-poor (which implies In-rich) and O-rich (which implies In-poor) conditions. For O-poor conditions, μ_{In} was equal to the energy of bulk In metal; for O-rich conditions, μ_O corresponded to the energy of O in a gaseous oxygen molecule. The calculated cohesive energy per O_2 molecule (−5.16 eV) was in good agreement with the experimental ones (−5.23 eV).[56] Details of chemical potentials used to calculate defect formation energies for different doped species along with the calculated formation enthalpies of possible secondary phases are provided in Tables S1 and S2 (Supporting Information). Taking Mo-doped In_2O_3 as examples, the In and O potentials have to fulfill the stability condition for bulk In_2O_3

$$2\mu_{In} + 3\mu_O = E_{In_2O_3} \quad (3)$$

$$\mu_{In} \leq E_{In} \quad (4)$$

$$\mu_O \leq E_O \quad (5)$$

The Mo chemical potential will determine the doping level

$$\mu_{Mo} + 3\mu_O \leq \mu_{MoO_3} \quad (6)$$

Equilibrium Defect Concentrations: Under thermodynamic equilibrium conditions, the defect concentrations depend on their formation energies, degeneracy factor, and the temperature, following Boltzmann distribution[57]

$$c = N_{sites}\, g_q \exp\left(-E^f\left[X^q\right]/k_B T\right) \quad (7)$$

Here, N_{sites} is the number of possible sites on which defect X can be incorporated per volume, k_B is Boltzmann's constant, T is the temperature, and g_q is the degeneracy factor that equals to the number of possible electron configurations for different charge states. With the constraint of charge neutrality condition

$$p_0 + \sum_i q_i\, n_{D_i}^{q_i^+} = n_0 + \sum_j q_j n_{A_j}^{q_j^-} \quad (8)$$

the defect density and the Fermi energy level can be calculated self-consistently as a function of the temperature and the growth chemical potentials.[57] $n_{D_i}^{q_i^+}$ is the density of a donor D_i with charge state $+q_i$, and $n_{A_j}^{q_j^-}$ is the density of an acceptor A_j with charge state $-q_j$. p_0 and n_0 are the thermally excited hole density and electron density, respectively

$$p_0 = N_v\, e^{-E_F/k_B T},\ N_v = 2\frac{(2\pi m_h^* k_B T)^{3/2}}{h^3} \quad (9)$$

$$n_0 = N_c e^{(E_F - E_g)/k_B T},\ N_c = 2\frac{(2\pi m_e^* k_B T)^{3/2}}{h^3} \quad (10)$$

where N_v and N_c are the effective density of states of the valence band and the conduction band. m_e^* and m_h^* are the effective masses for electron and hole, respectively.

In practice, TCO films grew under relatively high temperature but worked at room temperature. Therefore, thermal quenching was often used to enhance the carrier density, where the defect concentrations obtained at the growth temperature were frozen-in at room temperature.[58] However, the defect densities at different charge states along with the equilibrium E_F will be redistributed. For example, considering a defect X with three charge states 0, 1+, and 2+, the defect densities of X^0, X^{1+}, and X^{2+} after quenching to WT are recalculated as

$$c'\left(X^0\right) = N_X \frac{g_0 \exp\left(-\dfrac{E^f\left[X^0\right]}{k_B(WT)}\right)}{g_0 \exp\left(-\dfrac{E^f\left[X^0\right]}{k_B(WT)}\right) + g_{1+} \exp\left(-\dfrac{E^f\left[X^{1+}\right]}{k_B(WT)}\right) + g_{2+} \exp\left(-\dfrac{E^f\left[X^{2+}\right]}{k_B(WT)}\right)} \quad (11)$$

$$c'\left(X^{1+}\right) = N_X \frac{g_0 \exp\left(-\dfrac{E^f\left[X^{1+}\right]}{k_B(WT)}\right)}{g_0 \exp\left(-\dfrac{E^f\left[X^0\right]}{k_B(WT)}\right) + g_{1+} \exp\left(-\dfrac{E^f\left[X^{1+}\right]}{k_B(WT)}\right) + g_{2+} \exp\left(-\dfrac{E^f\left[X^{2+}\right]}{k_B(WT)}\right)} \quad (12)$$

$$c'\left(X^{2+}\right) = N_X \frac{g_0 \exp\left(-\dfrac{E^f\left[X^{2+}\right]}{k_B(WT)}\right)}{g_0 \exp\left(-\dfrac{E^f\left[X^0\right]}{k_B(WT)}\right) + g_{1+} \exp\left(-\dfrac{E^f\left[X^{1+}\right]}{k_B(WT)}\right) + g_{2+} \exp\left(-\dfrac{E^f\left[X^{2+}\right]}{k_B(WT)}\right)} \quad (13)$$

$$N_X = N_{sites}\left[g_0 \exp\left(-\frac{E^f[X^0]}{k_B(GT)}\right) + g_{1+} \exp\left(-\frac{E^f[X^{1+}]}{k_B(GT)}\right) + g_{2+} \exp\left(-\frac{E^f[X^{2+}]}{k_B(GT)}\right)\right]$$

(14)

where N_X is fixed as the sum of the densities of X with all possible charge states at GT. By solving Equations (1) and (8)–(14) self-consistently, a new set of carrier densities, E_F and defect densities can be obtained with different charge states after quenching to WT.

Supporting Information

Supporting Information is available from the Wiley Online Library or from the author.

Conflict of Interest

The authors declare no conflict of interest.

[1] A. Klein, *J. Am. Ceram. Soc.* **2013**, *96*, 331.
[2] S. Calnan, A. N. Tiwari, *Thin Solid Films* **2010**, *518*, 1839.
[3] A. Porch, D. V. Morgan, R. M. Perks, M. O. Jones, P. P. Edwards, *J. Appl. Phys.* **2004**, *95*, 4734.
[4] C. G. Granqvist, A. Hultåker, *Thin Solid Films* **2002**, *411*, 1.
[5] J. Gao, K. Kempa, M. Giersig, E. M. Akinoglu, B. Han, R. Li, *Adv. Phys.* **2016**, *65*, 553.
[6] A. M. Schimpf, S. D. Lounis, E. L. Runnerstrom, D. J. Milliron, D. R. Gamelin, *J. Am. Chem. Soc.* **2015**, *137*, 518.
[7] O. Mryasov, A. Freeman, *Phys. Rev. B* **2001**, *64*, 233111.
[8] A. Walsh, J. L. F. Da Silva, S.-H. Wei, *Phys. Rev. B* **2008**, *78*, 075211.
[9] M. Lundstrom, *Fundamentals of Carrier Transport*, Cambridge University Press, London **2009**.
[10] K. Ellmer, R. Mientus, *Thin Solid Films* **2008**, *516*, 5829.
[11] K. Ellmer, *J. Phys. D: Appl. Phys.* **2001**, *34*, 3097.
[12] S. K. Vishwanath, K. Y. Cho, J. Kim, *J. Phys. D: Appl. Phys.* **2016**, *49*, 155501.
[13] A. Song, H.-W. Park, S. K. Vishwanath, J. Kim, J.-Y. Baek, K.-J. Ahn, K.-B. Chung, *Ceram. Int.* **2016**, *42*, 14754.
[14] O. Lozano, Q. Y. Chen, P. V. Wadekar, H. W. Seo, P. V. Chinta, L. H. Chu, L. W. Tu, I. Lo, S. W. Yeh, N. J. Ho, F. C. Chuang, D. J. Jang, D. Wijesundera, W.-K. Chu, *Sol. Energy Mater. Sol. Cells* **2013**, *113*, 171.
[15] S. Parthiban, E. Elangovan, K. Ramamurthi, R. Martins, E. Fortunato, *Sol. Energy Mater. Sol. Cells* **2010**, *94*, 406.
[16] M. Yang, J. Feng, G. Li, Q. Zhang, *J. Cryst. Growth* **2008**, *310*, 3474.
[17] R. K. Gupta, K. Ghosh, S. R. Mishra, P. K. Kahol, *Appl. Surf. Sci.* **2008**, *254*, 1661.
[18] R. K. Gupta, K. Ghosh, S. R. Mishra, P. K. Kahol, *Mater. Lett.* **2008**, *62*, 1033.
[19] T. Koida, M. Kondo, *J. Appl. Phys.* **2007**, *101*, 063705.
[20] J. H. Kim, Y.-H. Shin, T.-Y. Seong, S.-I. Na, H.-K. Kim, *J. Phys. D: Appl. Phys.* **2012**, *45*, 395104.
[21] T. A. Gessert, Y. Yoshida, C. C. Fesenmaier, T. J. Coutts, *J. Appl. Phys.* **2009**, *105*, 083547.
[22] T. J. Peshek, J. M. Burst, T. J. Coutts, T. A. Gessert, *J. Vac. Sci. Technol., A* **2016**, *34*, 021201.
[23] A. W. Jansons, K. M. Koskela, B. M. Crockett, J. E. Hutchison, *Chem. Mater.* **2017**, *29*, 8167.
[24] Y. Meng, X.-L. Yang, H.-X. Chen, J. Shen, Y.-M. Jiang, Z.-J. Zhang, Z.-Y. Hua, *Thin Solid Films* **2001**, *394*, 218.
[25] Y. Yoshida, T. A. Gessert, C. L. Perkins, T. J. Coutts, *J. Vac. Sci. Technol., A* **2003**, *21*, 1092.
[26] D. S. Bhachu, D. O. Scanlon, G. Sankar, T. D. Veal, R. G. Egdell, G. Cibin, A. J. Dent, C. E. Knapp, C. J. Carmalt, I. P. Parkin, *Chem. Mater.* **2015**, *27*, 2788.
[27] N. Beji, M. Souli, M. Reghima, S. Azzaza, A. Safia, N. Kamoun-Turki, *J. Electron. Mater.* **2017**, *46*, 6628.
[28] S.-Y. Sun, J.-L. Huang, D.-F. Lii, *Thin Solid Films* **2004**, *469*, 6.
[29] S.-Y. Sun, J.-L. Huang, D.-F. Lii, *J. Mater. Res.* **2005**, *20*, 247.
[30] X. Li, W. Miao, Q. Zhang, L. Huang, Z. Zhang, Z. Hua, *Semicond. Sci. Technol.* **2005**, *20*, 823.
[31] E. Elangovan, R. Martins, E. Fortunato, *Thin Solid Films* **2007**, *515*, 8549.
[32] J. E. Medvedeva, *Phys. Rev. Lett.* **2006**, *97*, 086401.
[33] B. Huang, H. Xiang, J. Yu, S. H. Wei, *Phys. Rev. Lett.* **2012**, *108*, 206802.
[34] D. J. Chadi, K. J. Chang, *Phys. Rev. Lett.* **1988**, *61*, 873.
[35] Y. Ohhata, F. Shinoki, S. Yoshida, *Thin Solid Films* **1979**, *59*, 255.
[36] T. Koida, M. Kondo, *Appl. Phys. Lett.* **2006**, *89*, 082104.
[37] A. E. Delahoy, S. Y. Guo, *J. Vac. Sci. Technol., A* **2005**, *23*, 1215.
[38] T. Asikainen, M. Ritala, M. Leskelä, *Thin Solid Films* **2003**, *440*, 152.
[39] G. Kresse, J. Furthmüller, *Phys. Rev. B* **1996**, *54*, 11169.
[40] P. E. Blöchl, *Phys. Rev. B* **1994**, *50*, 17953.
[41] G. Kresse, D. Joubert, *Phys. Rev. B* **1999**, *59*, 1758.
[42] J. Heyd, G. E. Scuseria, M. Ernzerhof, *J. Chem. Phys.* **2003**, *118*, 8207.
[43] J. Paier, M. Marsman, K. Hummer, G. Kresse, I. C. Gerber, J. G. Ángyán, *J. Chem. Phys.* **2006**, *124*, 154709.
[44] A. V. Krukau, O. A. Vydrov, A. F. Izmaylov, G. E. Scuseria, *J. Chem. Phys.* **2006**, *125*, 224106.
[45] M. Marezio, *Acta Crystallogr.* **1966**, *20*, 723.
[46] V. Scherer, C. Janowitz, A. Krapf, H. Dwelk, D. Braun, R. Manzke, *Appl. Phys. Lett.* **2012**, *100*, 212108.
[47] A. Walsh, J. L. Da Silva, S. H. Wei, C. Korber, A. Klein, L. F. Piper, A. DeMasi, K. E. Smith, G. Panaccione, P. Torelli, D. J. Payne, A. Bourlange, R. G. Egdell, *Phys. Rev. Lett.* **2008**, *100*, 167402.
[48] A. Walsh, J. L. F. Da Silva, Y. Yan, M. M. Al-Jassim, S.-H. Wei, *Phys. Rev. B* **2009**, *79*, 073105.
[49] S. Lany, A. Zunger, *Phys. Rev. B* **2008**, *78*, 235104.
[50] C. Freysoldt, B. Grabowski, T. Hickel, J. Neugebauer, G. Kresse, A. Janotti, C. G. Van de Walle, *Rev. Mod. Phys.* **2014**, *86*, 253.
[51] S. Lany, A. Zunger, *Modell. Simul. Mater. Sci. Eng.* **2009**, *17*, 084002.
[52] C. G. Van de Walle, J. Neugebauer, *J. Appl. Phys.* **2004**, *95*, 3851.
[53] C. Freysoldt, B. Lange, J. Neugebauer, Q. Yan, J. L. Lyons, A. Janotti, C. G. Van de Walle, *Phys. Rev. B* **2016**, *93*, 165206.
[54] F. Gallino, G. Pacchioni, C. Di Valentin, *J. Chem. Phys.* **2010**, *133*, 144512.
[55] Y. G. Yu, X. Zhang, A. Zunger, *Phys. Rev. B* **2017**, *95*, 085201.
[56] J. A. Pople, M. Head-Gordon, D. J. Fox, K. Raghavachari, L. A. Curtiss, *J. Chem. Phys.* **1989**, *90*, 5622.
[57] J. Ma, S.-H. Wei, T. A. Gessert, K. K. Chin, *Phys. Rev. B* **2011**, *83*, 245207.
[58] J.-H. Yang, J.-S. Park, J. Kang, W. Metzger, T. Barnes, S.-H. Wei, *Phys. Rev. B* **2014**, *90*, 245202.